Simulating transcranial direct current stimulation with a detailed anisotropic human head model

Sumientra M. Rampersad, Arno M. Janssen, Felix Lucka, Ümit Aydin, Benjamin Lanfer, Seok Lew, Carsten H. Wolters, Dick F. Stegeman, Thom F. Oostendorp

***Abstract*—Transcranial direct current stimulation (tDCS) is a non-invasive brain stimulation technique able to induce long-lasting changes in cortical excitability that can benefit cognitive functioning and clinical treatment. In order to both better understand the mechanisms behind tDCS and possibly improve the technique, finite element models are used to simulate tDCS of the human brain. With the detailed anisotropic head model presented in this study, we provide accurate predictions of tDCS in the human brain for six of the practically most-used setups in clinical and cognitive research, targeting the primary motor cortex, dorsolateral prefrontal cortex, inferior frontal gyrus, occipital cortex and cerebellum. We present the resulting electric field strengths in the complete brain and introduce new methods to evaluate the effectivity in the target area specifically, where we have analyzed both the strength and direction of the field. For all cerebral targets studied, the currently accepted configurations produced sub-optimal field strengths. The configuration for cerebellum stimulation produced relatively high field strengths in its target area, but it needs higher input currents than cerebral stimulation does. This study suggests that improvements in the effects of transcranial direct current stimulation are achievable.**

***Index Terms*—transcranial direct current stimulation (tDCS), finite element model (FEM), motor cortex, prefrontal cortex, occipital cortex, cerebellum**

Manuscript received October 6, 2013; revised February 11, 2014.

The authors gratefully acknowledge the support of the BrainGain Smart Mix Programme of the Netherlands Ministry of Economic Affairs and the Netherlands Ministry of Education, Culture and Science. It was further supported by funding awarded to CW from the German Research Foundation (DFG WO1425/2-1 and 5-1) for ÜA and from BESA GmbH, Gräfelfing, Germany for BL. FL was funded by the German National Academic Foundation (Studienstiftung des deutschen Volkes). SL was funded by NIH (NIH grant R01EB0009048). The study was made possible in part by software that is developed with the support of grants from the National Center for Research Resources (5P41RR012553-15) and the National Institute of General Medical Sciences (8 P41 GM103545-15) from the National Institutes of Health.

SR and AJ are with the Department of Neurology of the Radboud University Nijmegen Medical Center and the Donders Institute for Brain, Cognition and Behaviour in Nijmegen, the Netherlands.

FL is with the Institute for Biomagnetism and Biosignalanalysis and the Institute for Computational and Applied Mathematics of the University of Münster in Münster, Germany.

ÜA and CW are with the Institute for Biomagnetism and Biosignalanalysis of the University of Münster in Münster, Germany.

BL is with the Institute for Biomagnetism and Biosignalanalysis of the University of Münster in Münster, Germany and BESA GmbH in Gräfelfing, Germany.

SL is with the Athinoula A. Martinos Center for Biomedical Imaging Massachusetts General Hospital of Harvard Medical School in Boston, USA.

DS is with the Department of Neurology of the Radboud University Nijmegen Medical Center and the Donders Institute for Brain, Cognition and Behaviour in Nijmegen, the Netherlands, and with the Faculty of Human Movement Sciences and MOVE Research Institute of VU University, Amsterdam, the Netherlands (email: Dick.Stegeman@radboudumc.nl).

TO is with the Department of Cognitive Neuroscience of the Radboud University Nijmegen Medical Center and the Donders Institute for Brain, Cognition and Behaviour in Nijmegen, the Netherlands.

I. Introduction

TRANSCRANIAL direct current stimulation (tDCS) is a non-invasive brain stimulation technique that has gained increasing interest over the past two decades. The most-used form of stimulation uses two large planar electrodes on the scalp to send a weak direct current through the brain [1]. This technique can induce a polarity-dependent change in excitability in the stimulated brain area that can last for hours after stimulation, depending on stimulation time [2], [3]. Applied to the motor cortex, this effect has been employed to improve motor function after stroke [4] and to aid in the treatment of other neuropathologies [5]. Targeting other brain areas, positive effects of tDCS are evident via parameters as mood status [6] and performance in tasks involving memory [7] or other cognitive functions [8]. In order to both better understand the mechanisms behind tDCS and possibly improve the technique, we first need to know the distribution of the electric field in the brain. This information can be found through simulations of tDCS with a realistic volume conduction model of the head. In this study, we aimed to create one highly detailed model that includes all relevant features and use it to simulate the most commonly used setups.

To achieve the highest amount of accuracy, a volume conduction model needs a detailed description of the geometry of the structures in the head and the conductivity properties of each tissue. As the quality of magnetic resonance images (MRI) and the performance of computers increased, models included more different tissue types, a higher level of detail in geometry and realistic representations of anisotropically conducting tissues. In some studies, the three different layers of the skull were modeled explicitly [9] or by means of an anisotropic approximation [10]. Currently, models exist that consist of several million elements of either hexahedral [11], [12] or tetrahedral shape [13], [14], the latter resulting in smooth tissue boundaries. Investigators started using diffusion tensor imaging (DTI) to incorporate realistic fiber directions into their models, for white matter alone [10], [15] or for both gray and white matter [14]. All in all, many important details of tDCS volume conduction have been modeled accurately, but to our knowledge, our study is the first to include all these aspects into one model.

Most tDCS modeling studies have focused on motor cortex stimulation [13], [34], [35], [14]. For prefrontal cortex [11], [36] and occipital cortex [37], [36], a few modeling studies exist. Realistic simulations of other commonly used configurations have not been published before. In this study,

TABLE I
THE SIX CONFIGURATIONS SIMULATED IN THIS STUDY AND THEIR APPLICATIONS AS FOUND IN RECENT LITERATURE.

	Anode	Cathode	Application
A	M1[a] left	SO[f] right	motor recovery [16], pain [17], smoking [18]
B	DLPFC[b] left	SO[f] right	appetite [19], depression [20], emotion [21], memory [7], pain [22], problem solving [8]
C	DLPFC[b] left	DLPFC[b] right	addiction [23], cortisol [24], depression [6], tinnitus [25]
D	IFG[c] left	SO[f] right	apraxia [26], behavioral inhibition [27], language [28], motor resonance [29]
E	Oz[de]	Cz[e]	migraine [30], visual recovery [31]
F	cerebellum right	cheek right	cerebello-brain inhibition [32], motor adaptation [33]

[a]primary motor cortex; [b]dorsolateral prefrontal cortex; [c] inferior frontal gyrus; [d]occipital cortex; [e]as determined in the standardized 10-20 system for electrode placement; [f]supraorbital area

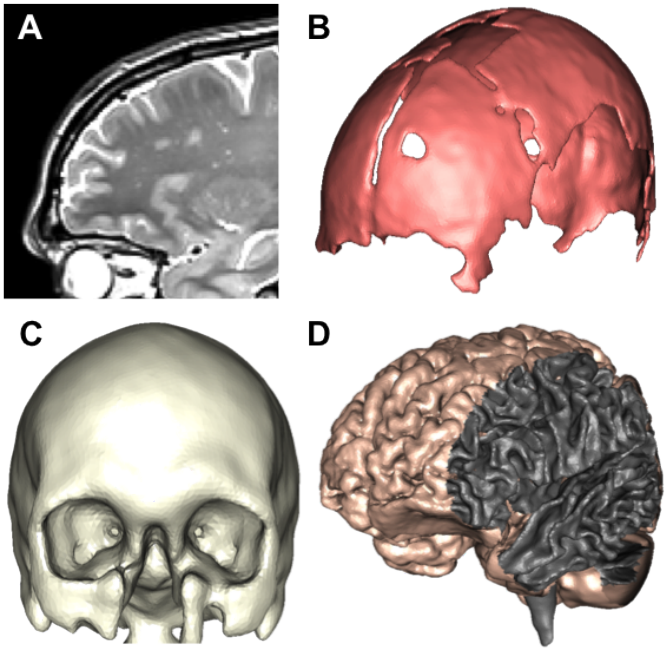

Fig. 1. Details of the volume conduction model used in this study. A) T2-weighted MRI, clearly showing skull spongiosa, B) spongiosa surface, C) outer skull surface with optic canals, D) surfaces of the cerebral and cerebellar gray and white matter and the brainstem.

we simulated tDCS for six 'standard' electrode configurations that are commonly used in clinical and cognitive research (see Table I).

We will present resulting electric fields in the brain, and in the target area specifically, where we have analyzed both the strength and direction of the field. These analyses show that for all cerebral targets studied, the currently accepted configurations lead to sub-optimal field strengths, while the standard configuration for cerebellar tDCS performs relatively well. Based on these results, we will discuss novel configurations that perform better than the standard configurations do.

II. METHODS

The volume conduction problem posed by tDCS can be described by the quasi-static Maxwell equations, which lead to Laplaces equation $\nabla \cdot \boldsymbol{\sigma} \nabla \Phi = 0$ within the volume in absence of current sources, with $\boldsymbol{\sigma}$ and Φ the electric conductivity and potential, respectively. As this equation cannot be solved analytically for a complicated geometry such as the head, the finite element method (FEM) can be used. The FEM dictates splitting the geometry into a mesh of small regular elements and solving the equation for each element separately but in relation to each other. For this study, a mesh of tetrahedral elements was constructed that reflects both the geometry and the conductive properties of the head in much detail. The creation of this realistic volume conduction model is described below. Afterwards we will delineate how tDCS was simulated with this model and finally the methods of analysis used in this study are presented.

A. Volume conduction model

A detailed anisotropic volume conduction model was constructed based on MR images of the head of a healthy 25-year old male subject. Written informed consent was obtained prior to scanning. T1- and T2-weighted images were used to reconstruct realistic geometries of the skin, skull compacta, skull spongiosa, cerebrospinal fluid (CSF), cerebral gray (GM) and white matter (WM), cerebellar gray (cGM) and white matter (cWM), brainstem, eyes and neck muscles, in the form of a triangular surface mesh for each tissue type. These surfaces were then combined into one tetrahedral volume mesh. In brain tissue, current tends to flow along the neuronal fiber direction. This behavior can be reconstructed by modeling brain tissue with anisotropic conductivity tensors. It has been shown that, primarily in the WM, currents in the model will follow known fiber paths [10], [38]. To estimate the anisotropic conductivity tensors of the brain tissue, we used the assumption that the conductivity tensors share eigenvectors with the diffusion tensors that can be measured via diffusion tensor imaging (DTI) [39], [40], [41]. Anisotropic conductivity was included for both gray and white matter of cerebrum and cerebellum. Some important features of the model are shown in Figure 1. The creation process of the model is visualized schematically in Figure 2 and details are provided below.

1) MRI acquisition: T1-, T2- and diffusion-weighted (DW) MR images were measured on a 3T MR scanner (Magnetom Trio, Siemens, Munich, Germany) with a 32-channel head coil. The T1-weighted (T1w) image was acquired with an MP-RAGE pulse sequence (TR = 2300 ms, TE = 3.03 ms, TI = 1100 ms, flip angle = 8 degrees, FOV = 256 x 256 x 192 mm, voxel size = 1 x 1 x 1 mm) with fat suppression and GRAPPA parallel imaging (acceleration factor = 2). The T2-weighted (T2w) image was acquired with an SPC pulse sequence (TR

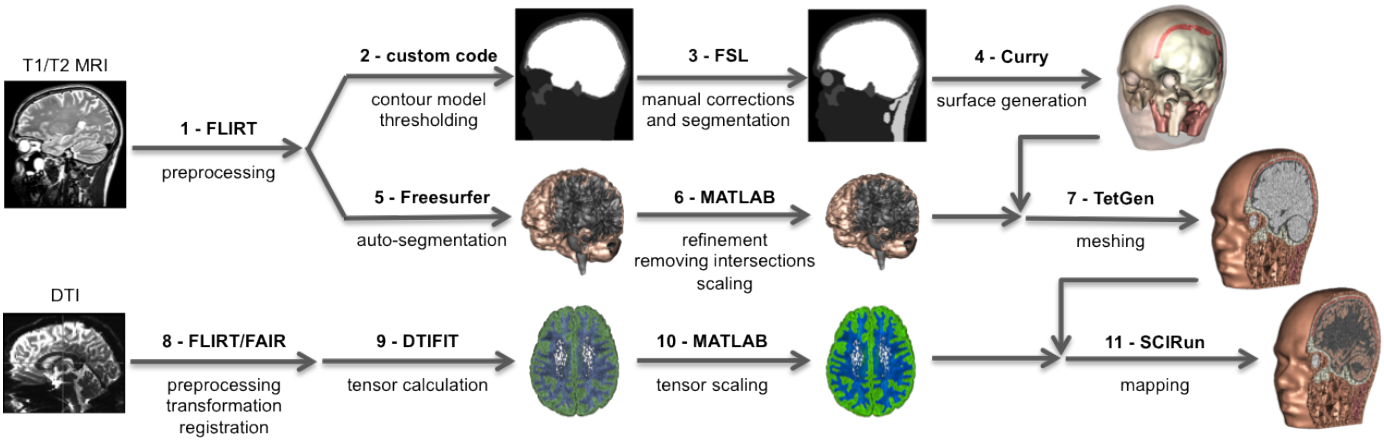

Fig. 2. Flowchart showing the creation process of the volume conduction model used in this study. T1- and T2-weighted MR images were preprocessed (1) and after automatic (2) and manual segmentations (3), triangular surface meshes were created for the skin, skull compacta and spongiosa, neck muscles and eyes (4). Surfaces for the cerebral and cerebellar gray and white matter and the brainstem were extracted from Freesurfer (5) and refined, made free of intersections and scaled with MATLAB and the iso2mesh toolbox (6). All surfaces were then combined into a tetrahedral volume mesh (7). Diffusion tensor imaging data was preprocessed, transformed and registered to the T1w/T2w scans (8), after which diffusion tensors (9) and conductivity tensors (10) were calculated. Finally, the conductivity tensors were mapped onto the mesh from (7) to result in a detailed tetrahedral mesh with conductivity tensors (11).

= 2000 ms, TE = 307 ms, FOV = 255 x 255 x 176 mm, voxel size = 0.99 x 1.0 x 1.0 mm interpolated to 0.498 x 0.498 x 1.00 mm). The T2w sequence was adjusted such that it gives a high contrast between the different layers of the skull. Figure 1A shows a section of a sagittal slice of the T2w scan, clearly showing the spongiosa layer. The field of view of both scans captured the complete head and was cut as low as the chin.

2) DTI acquisition: The DW images were acquired with the standard Siemens pulse sequence ep2d_diff (TR = 7700 ms, TE = 89 ms, b-value = 1000 s/mm^2, bandwidth = 2000 Hz/pixel, FOV = 220 x 220 x 141 mm, voxel size = 2.2 x 2.2 x 2.2 mm) in 61 directions equally distributed on a sphere and 7 images were acquired with flat diffusion gradient (diffusion weighting factor b = 0 (b0+)). Additionally, seven images with flat diffusion gradient (diffusion weighting factor b = 0 (b0-)) with reversed phase and frequency encoding gradients were acquired.

3) Segmentation: The T2w MRI was registered onto the T1w MRI using a rigid registration approach and mutual information as a cost-function as implemented in FSL[1] (→1, refers to arrow 1 in Figure 2). The compartments skin, skull compacta and skull spongiosa were then segmented from the registered T1w and T2w images using a gray-value based active contour model [42] and thresholding techniques (→2). These segmentations were carefully checked and corrected manually to ensure the highest possible agreement with the MR images and make sure the different tissues form closed surfaces. Eye, muscle and vertebrae segmentations were added manually. The foramen magnum and the two optic canals were modeled as skull openings (→3). Exemplary sagittal slices of both the automatic segmentation and manual alterations can be seen in the flowchart in Figure 2 after arrow 2 and arrow 3, respectively. The segmentation of GM, WM, cGM, cWM and brainstem was extracted from brain parcellation data of the T1w image created with Freesurfer[2] software (→5).

4) Triangular surface meshes: The software package CURRY[3] was used for the extraction of high resolution triangular surface meshes of the skin, eyes, compacta, spongiosa and muscles from the voxel-based segmentation volumes (→4). The surfaces were smoothed using Taubin smoothing [43] to remove the blocky structure which results from the fine surface sampling of the voxels.

Triangular surface meshes of all brain parcellations were made in MATLAB and refined using the package iso2mesh[4] [44]. As Freesurfer produces separate segmentations for each hemisphere, the hemispheres were connected and self-intersections were removed with custom MATLAB code. In the subsequent step of this process - creation of a volume mesh from the surface meshes - the surfaces are not allowed to touch. Therefore, the part of the WM surface that extended out of the GM surface especially in the inferior brain region was identified and corrected using the custom code. To avoid intersections between the gray matter and compacta surfaces, the complete brain was scaled down by 2% and flattened at remaining intersections (→6). Figure 1 shows the detailed spongiosa surface (B), the skull surface with the optic canals (C) and all five brain surfaces (D).

5) Tetrahedral volume meshes: The smoothed surfaces (skin, compacta, spongiosa, GM, WM, cGM, cWM, brainstem, left eye, right eye, muscle) were used to create a high quality 3D Delaunay triangulation via TetGen[5] (→7). This resulted in a mesh consisting of 672k nodes and 4.12M linear tetrahedral elements. The element size in the brain was restricted to 1 mm^3. Due to the use of detailed surfaces, the elements of the skull and CSF compartments are very small as well. To all

[1]FLIRT (FMRIB's Linear Image Registration Tool) is part of FSL (FMRIB Software Library), which is freely available at http://www.fmrib.ox.ac.uk.

[2]Freesurfer is freely available at http://surfer.nmr.mgh.harvard.edu.

[3]CURRY (CURrent Reconstruction and Imaging), Compumedics, Charlotte, NC, USA, http://www.neuroscan.com

[4]The package iso2mesh is freely available at http://iso2mesh.sourceforge.net/cgi-bin/index.cgi.

[5]TetGen (A Quality Tetrahedral Mesh Generator and a 3D Delaunay Triangulator) is freely available at http://tetgen.org.

TABLE II
TISSUES REPRESENTED IN OUR MODEL AND CONDUCTIVITIES USED FOR EACH COMPARTMENT. CONDUCTIVITIES DENOTED WITH AN ASTERISK ARE EFFECTIVE CONDUCTIVITIES OF THE VOLUME-NORMALIZED TENSORS OF THE ANISOTROPICALLY MODELED TISSUES [48].

Tissue	Conductivity (S/m)	Reference
skin	0.465	[36]
compacta	0.007	[49]
spongiosa	0.025	[49]
CSF	1.65	[36]
GM, cGM	0.276*	[36]
WM, cWM	0.126*	[36]
brainstem	0.201*	average GM/WM
eye	1.5	[50]
muscle	0.4	[51]

elements in the space between two surfaces, or inside a closed surface, a tissue index was assigned. We used an additional closed skull surface to label all elements within this skull surface that are not part of the brain compartments, as CSF.

6) Conductivity tensors: The diffusion-weighted MR images were corrected for eddy current (EC) artifacts by affinely registering each directional image to the average b0+ image using the FSL routine FLIRT[1]. After EC correction, the gradient directions were reoriented by multiplying them with the rotational part of the transformation matrix [45]. In order to correct for susceptibility artifacts, we used a reversed gradient approach that uses the averaged b0+ and b0- images to compute smooth and diffeomorphic geometric transformations using a problem-adapted multiscale nonlinear image registration procedure [46]. This approach is implemented in the FAIR toolbox[6]. The EC and susceptibility corrections allowed a simple rigid registration of the artifact-corrected averaged b0 image to the T2w image (which was already registered to the T1w image in a previous step) using FLIRT. The transformation matrix obtained in this step was then used to register the directional images to the T2w image (which is in T1 space). The corresponding gradient directions were also reoriented accordingly. From the artifact-corrected and registered DW images ($\rightarrow$8) the diffusion tensors were calculated using the FSL routine DTIFIT[7] [47] ($\rightarrow$9). Next, conductivity tensors were calculated from these diffusion tensors using the volume-normalized approach, as described in detail by [48] ($\rightarrow$10). The normalized eigenvectors were multiplied with the effective conductivities of the tissues for GM, WM and brainstem separately [48]. The conductivity values for all tissues used in this study can be found in Table II. In the last step, the conductivity tensors were mapped from the MRI voxels onto the GM, WM, cGM, cWM and brainstem compartments of the tetrahedral head mesh described above ($\rightarrow$11).

B. Simulating tDCS

In order to simulate the effects of tDCS on the above described volume conduction model, electrodes need to be built onto the model (sections II-B1 and II-B2) and boundary conditions have to be set, after which the problem can be solved (section II-B3).

[6]FAIR (Flexible Algorithms for Image Registration) is freely available at http://www.siam.org/books/fa06.

[7]DTIFIT is part of FSL (FMRIB Software Library), which is freely available at http://www.fmrib.ox.ac.uk.

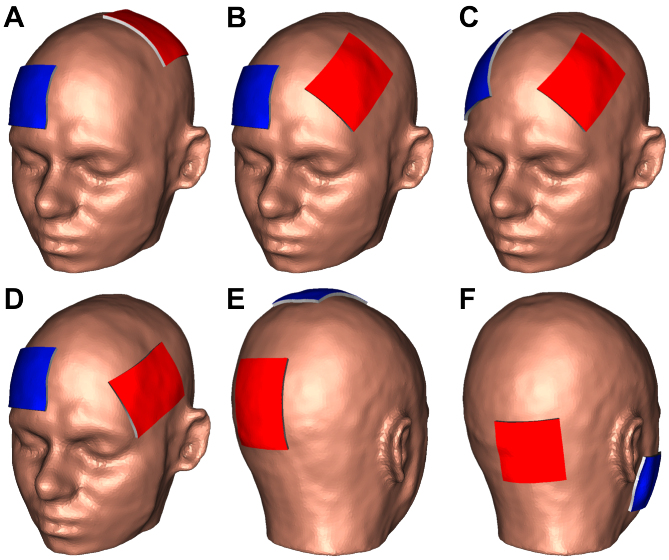

Fig. 3. The six standard tDCS configurations simulated in this study, targeting A) primary motor cortex, B) dorsolateral prefrontal cortex, C) both dorsolateral prefrontal cortices, D) inferior frontal gyrus, E) occipital cortex and F) cerebellum. The red surfaces indicate simulation of a positive potential $+\Phi_0$ for the anode and the blue surfaces indicate simulation of a negative potential $-\Phi_0$ for the cathode.

1) Electrode configurations: We modeled six commonly used configurations for tDCS. Table I gives an overview of the electrode locations for each configuration. Figure 3 shows all configurations as they were simulated in this study. To simulate motor cortex (M1) stimulation, the location of the cerebral representation of the first dorsal interosseus (FDI) muscle of the right hand was experimentally determined in the volunteer on which the model was based, via single-pulse transcranial magnetic stimulation (TMS) and electromyography (EMG). The location on the head that elicited the highest potential in the FDI muscle was accurately determined using neuronavigation software (Localite TMS Navigator[8]) and the T2w MRI data set that was used to create the model. The anode was centered over this location with its short edge parallel to the midline of the brain (Fig. 3-A). For configuration A, B and D, the supraorbital (SO) cathode was placed above the right eyebrow, not crossing the midline (Fig. 3-A,B,D). Both dorsolateral prefrontal cortices (DLPFC) and the inferior frontal gyrus (IFG) were located on the brain surface of the model based on anatomical knowledge and the electrodes were placed centered over the cortices covering the target area completely (Fig. 3-B,C,D). The Oz electrode was placed 4 cm above the inion, a point which was located on the skull surface of the model, and the Cz electrode was centered at the vertex, both with their long edges parallel to the midline of the brain (Fig. 3-E). For cerebellar stimulation, the square anode was placed with its center 3 cm right of the inion and the cathode was placed on the middle of the right cheek (Fig. 3-F) [32], [33].

[8]Localite GmbH, Sankt Augustin, Germany, http://www.localite.de

2) Electrode geometry: The electrodes were modeled as sponges with a thickness of 3 mm and the conductivity of saline (1.4 S/m). The sizes of the electrodes were chosen to match common practice in recent experiments (see Table I). For the configurations with cerebral targets, the electrodes were 5 x 7 cm; for cerebellar stimulation, the electrodes were 5 x 5 cm. Straight edges of the electrodes were made by splitting tetrahedrons on the surface of the model with custom C++ code and adding six layers of tetrahedrons on top of the resulting rectangular patch. With this method, electrodes can be built easily onto a standard model and have the exact size and thickness desired. The nodes in the top layer of the anode were assigned a potential of $+\Phi_0$ and the top layer of the cathode was assigned $-\Phi_0$, with Φ_0 chosen such that the total current entering the skin is equal to 1 mA.

3) Calculations: Laplace's equation was solved on the finite element mesh described above with Neumann boundary conditions, $\boldsymbol{\sigma}\nabla\Phi \cdot \vec{n} = 0$, at the skin surface outside the electrodes and Dirichlet boundary conditions, $\Phi = \Phi_0$, on the surfaces of the electrodes. The system of equations was solved with the FEM solving package SCIRun 4.6[9] using a conjugent gradient solver and Jacobi preconditioner with a maximal residual of 10^{-10}. These calculations resulted in a potential Φ at each node of the finite element head mesh.

C. Analysis

From the potential Φ at the nodes of the mesh and the conductivity tensors $\boldsymbol{\sigma}$ at the elements, the electric field $\vec{E} = -\nabla\Phi$ and the current density $\vec{J} = \boldsymbol{\sigma}\vec{E}$ were calculated in each element. The distribution of the electric field was investigated 1) on the brain surface, 2) in the complete brain volume, and 3) in a small volume at the target location. In this section, for cerebral stimulation (configurations A-E) interchange *brain* with *cerebrum* and for cerebellar stimulation (configuration F) interchange *brain* with *cerebellum*.

1) Surface: At each target location, a 1 cm^2 circular patch was built into the gray matter surface mesh to find the current entering the gray matter exactly at the target location (I^{T}). We determined the maximum electric field strength over the GM surface ($|\vec{E}|^{\mathrm{S}}_{\mathrm{mx}}$), where the maximum was defined as the median of the 0.01% highest values. As a measure of focality, we calculated the surface area (A_{75}) at which the field strength is above 75% of $|\vec{E}|^{\mathrm{S}}_{\mathrm{mx}}$.

2) Volume: We determined the maximum electric field strength in the complete brain volume ($|\vec{E}|^{\mathrm{V}}_{\mathrm{mx}}$), where the maximum was defined as the median of the 0.01% highest values. As the curved cortex leads to multiple areas where the electric field is (near-) maximal, it is not possible to indicate *the* location of maximum electric field strength. Therefore, we provide distributions (histograms) of the electric field strength values in the complete brain volume. In order to understand the distribution of the electric field both close to the target and in the complete brain, all brain elements were divided into subsets based on the distance of their centers from the target. For each subset, we display a histogram of the electric field strengths $|\vec{E}|$ in the elements, expressed in volume fractions (sum of volumes of elements in a bin divided by total volume of subset). A schematic of this approach is shown in Figure 6A.

3) Target volume: In order to provide a measure of the effects of tDCS exactly in the targeted region, a target volume was constructed in the form of a cylindrical mesh with a 1 cm^2 base and 4 mm height. At each target location, such a cylinder was placed inside the gray matter adjacent to the surface, with its axis perpendicular to the GM surface. All GM elements within this cylinder were selected as the target volume at this location. The resulting target volume is thus a 1 cm^2 slab of cortex. Different dimensions of the target area were investigated and lead to slightly different values as expected (e.g. a thinner layer leads to higher average field strength, because deeper elements have lower field strengths), but the trend in the results was consistent. The mean ($|\vec{E}|^{\mathrm{T}}_{\mathrm{mn}}$) and maximum ($|\vec{E}|^{\mathrm{T}}_{\mathrm{mx}}$) field strength in a target volume were used as estimates of the effect of tDCS in the target area. Assuming that the effect of stimulation is highest if the electric field is directed parallel to the fibers [52], [53] and that GM neurons lie perpendicular to its surface [54], we also calculated the mean electric field strength normal to the GM surface. For each GM element in a target volume, we calculated the dot product of the electric field vector, $\vec{E}$, with the vector normal to the closest GM surface triangle, $\hat{n}$, and provide the mean value within the volume: $\vec{E} \cdot \hat{n}\,{}^{\mathrm{T}}_{\mathrm{mn}}$.

III. Results

Below we describe the results on the GM surface, in the complete brain volume and in the target volume separately. As tDCS volume conduction is a linear process, the results presented here can be scaled to any input current by multiplying the electric field strengths with the desired current in mA. Our results can therefore also be extrapolated to cathodal stimulation; this only reverses the polarity of the field.

A. Surface

Figure 4 shows the simulated electric field strength on the skin (A), skull (B) and GM (C) surfaces for dual DLPFC stimulation. Results for the other configurations on the skin and skull are similar and therefore not shown. Figure 5 shows the electric field strength on the surface of the gray matter for all six configurations. The target of stimulation is indicated with a black dot. On the skin surface (Fig. 4A), the electric field is high under the edges of both electrodes, with peaks at the corners. The highest values are found at the corners closest to the other electrode. On the surface of the skull (Fig. 4B) the highest values remain under the electrodes, but the distribution is more homogeneous. On the brain surface this distribution of high electric field strengths under both electrodes has merged into one more central area (Fig. 4C). For all five cerebral targets the peak electric field locations have shifted away from the electrodes and the maximum result of stimulation is found in between the two electrodes (Fig. 5). A large area of (near-)maximal electric field is spread over multiple gyri on both hemispheres, roughly centered on the

[9]SCIRun (Scientific Computing and Imaging Institute, Salt Lake City, UT, USA) is freely available at http://www.sci.utah.edu/cibc-software/scirun.html.

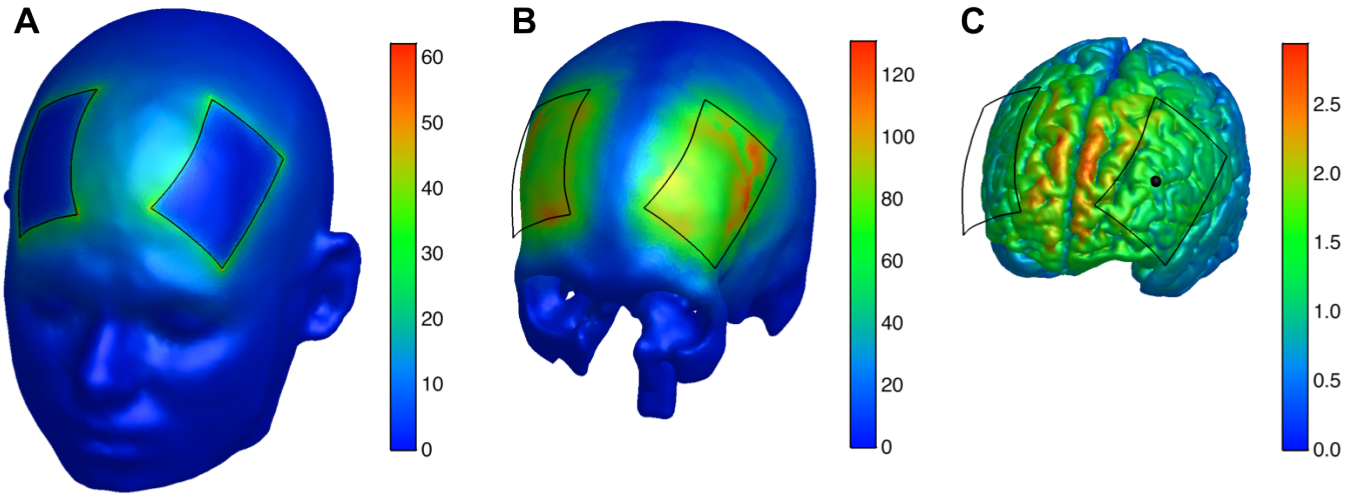

Fig. 4. Electric field strength $|\vec{E}|$ (mV/cm) on the surfaces of the A) skin, B) skull and C) GM for dual DLPFC stimulation (configuration C). The black outlines indicate the positions of the electrodes and the black dot indicates the target.

TABLE III
QUANTITATIVE RESULTS OF SIMULATING 1 MA TDCS FOR SIX CONFIGURATIONS.

	target	$\lvert\vec{E}\rvert^{\mathrm{S}}_{\mathrm{mx}}$ (mV/cm)	A_{75} (cm^2)	I^{T} (μA)	$\lvert\vec{E}\rvert^{\mathrm{V}}_{\mathrm{mx}}$ (mV/cm)	$\lvert\vec{E}\rvert^{\mathrm{T}}_{\mathrm{mx}}$ (mV/cm)	$\lvert\vec{E}\rvert^{\mathrm{T}}_{\mathrm{mn}}$ (mV/cm)	$\vec{E}\cdot\hat{n}^{\mathrm{T}}_{\mathrm{mn}}$ (mV/cm)
A	M1	2.9	7.3	3.0	2.9	2.1	1.4	1.2
B	DLPFC	2.8	5.7	2.4	3.1	1.7	1.2	0.86
C	DLPFC	2.7	10	2.4	3.3	1.7	1.3	0.87
D	IFG	2.4	6.7	2.6	2.7	1.7	1.1	0.86
E	Oz	3.2	1.9	1.5	3.4	1.5	0.85	0.55
F	cerebellum	1.1	1.5	1.9	1.2	0.88	0.75	0.71

From left to right: maximum electric field strength on the brain surface ($|\vec{E}|^{\mathrm{S}}_{\mathrm{mx}}$), surface area where 75% of the maximum surface value is reached (A_{75}), current entering the brain surface at the target location (I^{T}), maximum electric field strength in the brain volume ($|\vec{E}|^{\mathrm{V}}_{\mathrm{mx}}$), maximum electric field strength in the target volume ($|\vec{E}|^{\mathrm{T}}_{\mathrm{mx}}$), mean electric field strength in the target volume ($|\vec{E}|^{\mathrm{T}}_{\mathrm{mn}}$) and mean electric field strength perpendicular to the GM surface ($\vec{E}\cdot\hat{n}^{\mathrm{T}}_{\mathrm{mn}}$). Configurations B and C target the same area using a different reference location.

midline, with the highest values closer to the anode. For M1 stimulation this area is stretched along the coronal plane; for the prefrontal configurations it lies along the sagittal plane; for IFG and Oz stimulation the maximally stimulated areas are more circular. The simulations of cerebellum stimulation show a large patch of high electric field strength on the inferior surface of the right cerebellar hemisphere, covering the target area. In addition, an area of maximal electric field is found more inferior and medial on a highly concave surface area.

Maximum electric field strength values ($|\vec{E}|^{S}_{mx}$ in Table III) range from 2.4 to 3.2 mV/cm for the cerebral targets, while in the cerebellum a much lower maximum value of 1.1 mV/cm is reached. The values for the two DLPFC configurations hardly differ, but the surface area where at least 75% of this value is reached (A_{75} in Table III) is much larger for the dual DLPFC configuration, showing that this configuration is less focal. The Oz configuration leads to the largest maximum value and the smallest area receiving this field strength, showing a spatially sharp development of the high peak current. This configuration also leads to the smallest amount of current entering the GM at the target location (I^{T} in Table III).

B. Volume

For the cerebral targets, maximum electric field values in the complete brain ($|\vec{E}|^{\mathrm{V}}_{\mathrm{mx}}$ in Table III) between 2.7 and 3.4 mV/cm are reached, for IFG and Oz stimulation, respectively. The maximum field strength reached in the cerebellum is 1.2 mV/cm.

In Figure 6 we present distributions of the electric field strength in the complete brain (Fig. 6B) or cerebellum (Fig. 6C) for separate distance ranges to the target. For all frontal and motor targets (configurations A-D) we found relatively similar distributions and therefore only the results for DLPFC-SO stimulation (configuration B) are shown (Fig. 6B). Closest to the target (dark red curve) we see a sharp peak of high electric field strengths; further away from the target the distributions become broader and the peaks lie at lower values of $|\vec{E}|$. At the largest distance to the brain (dark blue curve) a sharp peak can be seen at low $|\vec{E}|$ values. Thus, close to the target mostly high values are found, far away mostly low values are found, and in between there is a wide range in the electric field strength. In all four cases, the highest field strengths are found at 20-40 mm from the target (note how the bright red curve spreads to higher values than all other curves do).

For Oz stimulation the peaks of the distributions at all

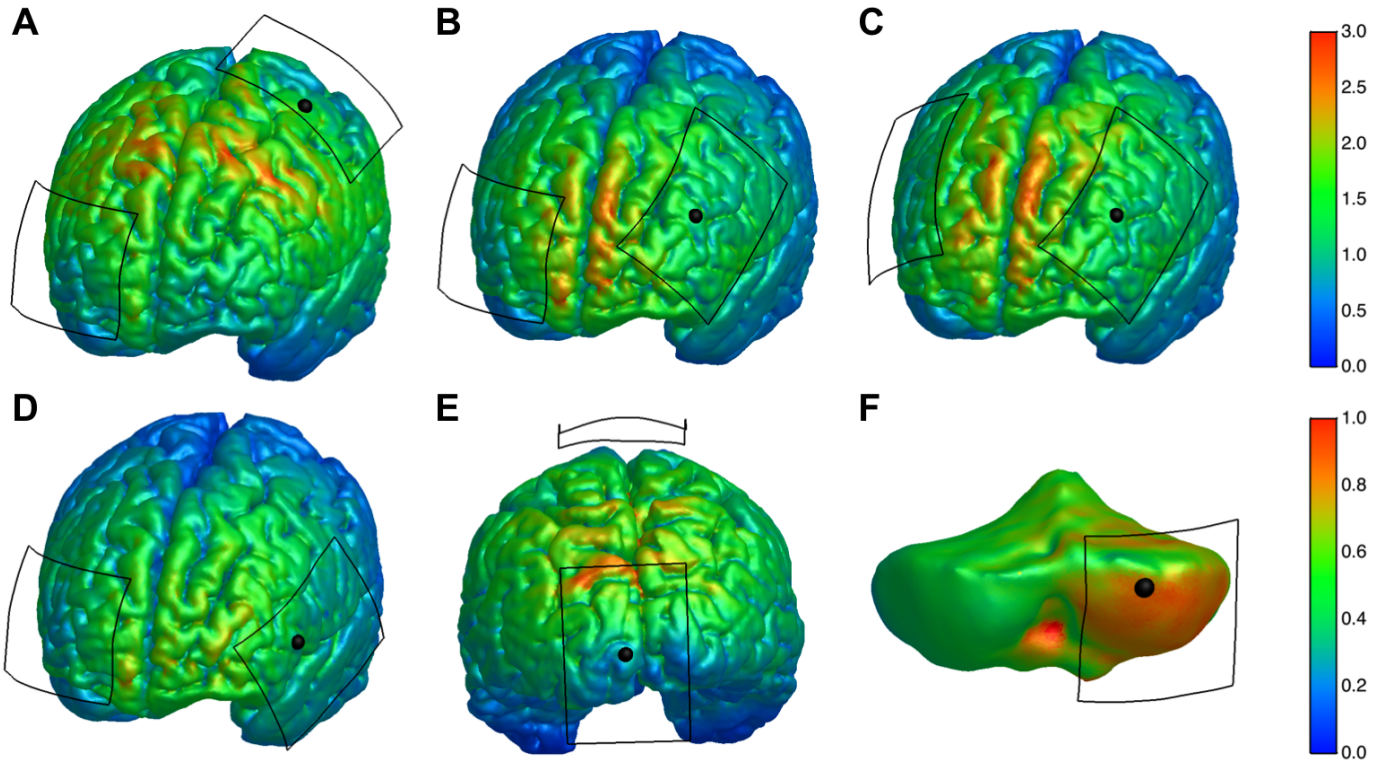

Fig. 5. Electric field strength $|\vec{E}|$ (mV/cm) on the surface of the GM for A) M1, B) left DLPFC, C) dual DLPFC, D) IFG and E) Oz stimulation, and on the surface of the cerebellum (F). Scales are adjusted (same scale for Figures A-E, shown at top right); actual maxima can be found in Table III. The black dot in each panel indicates the target of stimulation and the electrode-skin interface is outlined in black. The Oz target (E) was placed on the skin on the midline of the head, but due to the shape of the subjects brain, the target projection on the GM surface lies on the left hemisphere.

distances are similar, except for a sharp peak at the largest distance. In the cerebellum (Fig. 6C) the distributions are much narrower than for the cerebral targets and the peaks lie closer together and at lower values. This is due to the cerebellum being a much smaller and smoother structure than the brain. Highest electric field strengths are found in the elements closest to the target (0-20 mm).

Similar analyses were performed for gray and white matter separately, showing that for M1 and Oz stimulation the peaks of the distributions lie at higher $|\vec{E}|$ values in white matter than in gray matter. For all other configurations the locations of the peaks do not differ greatly between gray and white matter.

C. Target volume

The maximum field strength ($|\vec{E}|^{\mathrm{T}}_{\mathrm{mx}}$ in Table III) is 0.88 mV/cm in the cerebellar target volume, while in the cerebral target volumes $|\vec{E}|^{\mathrm{T}}_{\mathrm{mx}}$ ranges from 1.5 mV/cm for Oz to 2.1 mV/cm for M1 stimulation. For the two DLPFC configurations the maximum values reached in the target volume are 54-55% of the maximum value in the complete brain. For M1, IFG and cerebellum these values are 70, 62 and 76 %, respectively; for the Oz configuration it is only 45%. The average electric field strength in the target volumes ($|\vec{E}|^{\mathrm{T}}_{\mathrm{mn}}$ in Table III) ranges from 0.75 mV/cm for cerebellum to 1.4 mV/cm for M1 stimulation. The average electric field strength perpendicular to the GM surface ($\vec{E}\cdot\hat{n}\,^{\mathrm{T}}_{\mathrm{mn}}$ in Table III) ranges from 0.55 mV/cm for Oz to 1.2 mV/cm for M1 stimulation. While cerebellar stimulation resulted in relatively low values in several other analyses, the result for $\vec{E}\cdot\hat{n}\,^{\mathrm{T}}_{\mathrm{mn}}$ is similar to that of the other configurations. This is because the simulated electric field in the cerebellar target volume is mainly directed perpendicular to the GM surface.

IV. Discussion

This study presents simulations of 1 mA tDCS in a highly detailed volume conduction model for six commonly used electrode configurations.

A. General results

Highest electric field values in the skin were found along the rim of the electrodes, as was reported in other studies [55], [36], but here we also showed that the electric field distribution on the skull surface is high under the complete area of both electrodes and that a shift of the maximum away from the electrodes occurs only at brain level. As the current follows the path of least resistance, it is understandable that most current flows from the stimulator towards the edges of the electrodes to the skin instead of radially through the poorly conducting skull. A large part of the current goes from anode to cathode through the skin without passing the skull and thus never enters the brain. The current that does enter the skull spreads itself over its surface under the electrodes. When the current enters the CSF, it is transported through this highly conductive fluid away from the anode, leading to a wide distribution of the electric field on the brain surface. As we found only one area of maximal stimulation on the brain surface instead

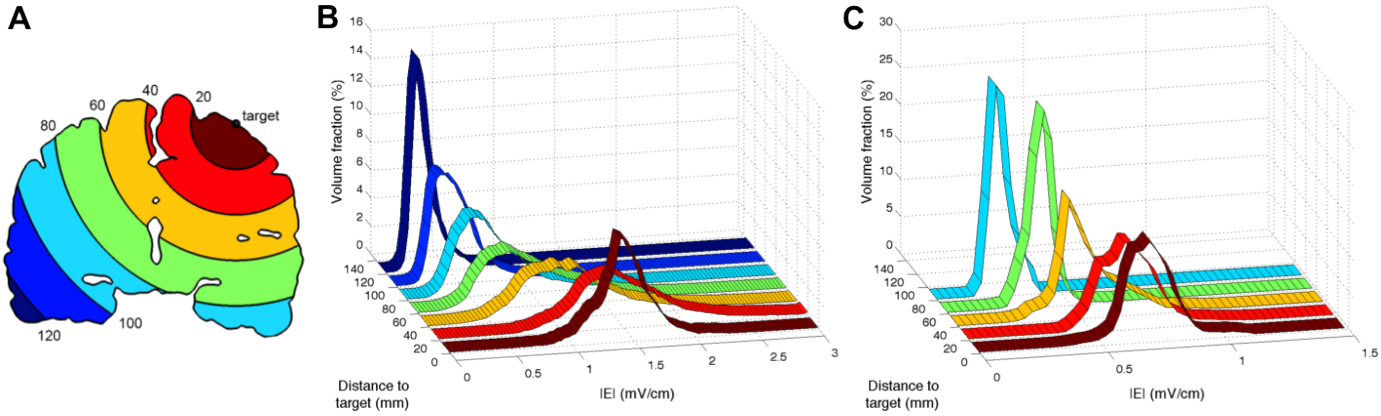

Fig. 6. Distribution of electric field strengths $|\vec{E}|$ (mV/cm) B) in the brain for DLPFC-SO and C) in the cerebellum for cerebellar stimulation. A) Schematic showing how these figures were created. All elements in the brain (or cerebellum for configuration F) were divided into subsets based on the distance of their centers to the target (shown in millimeters) and a histogram was made of the electric field strengths in each subset. The volumes of the elements are used to scale the distributions. Each histogram (per distance range) sums to 100%. The colors in the schematic correspond to the colors in the histograms.

of one under each electrode, this relieves possible worries for unwanted stimulation effects at the cathode. Our results suggest that the dimensions of the area of maximum field strength are determined by the length of the electrode edges that are facing each other. It thus seems possible to increase focality without changing the electrode size, simply by placing the electrodes with the short sides facing each other.

B. Cerebral targets

We simulated five configurations for four cerebral targets: left motor cortex, left dorsolateral prefrontal cortex, left inferior frontal gyrus and occipital cortex. For all cerebral targets we found large areas of near-maximal field strength located far away from the targets. Highest values were found 20-40 mm from the target, in between the anode and the cathode. Electric field strengths of more than twice the maximum value in the target volume are found in other brain areas. Not only is the target area not stimulated maximally, also other cerebral areas are stimulated much more strongly. Similar modeling results have been presented for M1 stimulation [13], [34] and for Oz stimulation in a stroke patient [37] using isotropic models. The results from our anisotropic model agree to these findings and show that also the standard configurations for DLPFC and IFG do not maximally stimulate their respective targets. Moreover, these results suggest that the common practice of placing electrodes over the target area leads to suboptimal field strengths.

Both DLPFC configurations lead to very similar results, not only at the targeted DLPFC, but also in the complete brain volume. Only the surface area A_{75} shows a large difference. The similar results for the two DLPFC configurations show that a small displacement of the return electrode for this target does not have a large influence on the resulting electric field.

In modeling studies it is common to report the value and surface area of maximum field strength. Our results indicate that in most cases these measures are not useful to determine effectivity and focality of a configuration. For example, the Oz configuration produced the highest field strengths and the most focal stimulation, while its effects in the targeted area were the smallest. For future modeling studies, it is therefore more useful to evaluate the electric field in a target volume.

C. Cerebellum

The configuration for cerebellum stimulation tested in this study resulted to be the only configuration that achieves relatively high electric field values at its target site. The actual maximum lies elsewhere, due to high local curvature, nevertheless the configuration seems near-optimal. The maximum of the electric field at the cerebellar surface is much lower than for the cerebral targets. This is probably due to large currents ducking inferiorly under the skull and flowing through the skin to the cheek. The Oz configuration also leads to low values in its target volume and a low inward current, while high values are achieved elsewhere. These results suggest that placing an electrode on the back of the head generally leads to large amounts of shunting. To achieve comparable field strengths in the cerebellum as reached with the other configurations, the input current for cerebellar stimulation should be doubled. In practical applications, most studies do use 2 mA tDCS for cerebellar stimulation [32], [33], [56].

D. Direction of the electric field

The above discussion focuses on areas of highest field strength, as is common in tDCS modeling studies [13], [11], [34]. In practice, the effects of stimulation might actually be higher in a different area, because the orientation of the field might have more significant effects than does the strength. The possible importance of field direction is already obvious from the fact that experiments have shown opposite effects of anodal versus cathodal tDCS [1]. For this reason, a measure of field directionality was analyzed in this study.

We found here that the standard configurations lead to maxima in field strength outside the target area. However, experimentally all these standard configurations have been shown to affect their targets. This could mean two things. As described above, if field strength is the most important parameter, then other areas are stimulated more strongly than

the target is. One would expect this to result in significant side-effects, something that has not been reported for tDCS. The other possibility is that electric field strength is not the parameter of interest. We have shown here that for the standard configurations a large part of the field is directed perpendicularly inward with respect to the GM surface. We also analyzed the perpendicular field strength in the areas of maximal absolute field strength (results not shown here) and found that in these areas (i.e. the red areas in Figure 5) the perpendicular field strength is much smaller than under the electrodes. The results for perpendicular field strength thus agree better with the experimental findings than the results for absolute field strength. Therefore, the direction of the field should be taken into account in future modeling studies. In order to better evaluate tDCS models, more knowledge on the effects of the fields direction versus its strength is needed.

E. Realistic modeling

In modeling tDCS, and other stimulation modalities in general, the ultimate goal would be to have individualized FE models made with the highest amount of accuracy. Due to the complicated nature of creating realistic tetrahedral anisotropic head models, this process is too time-consuming to create individual models. Simply converting an MRI scan directly into a hexahedral model is a fast method that does allow for individualized models, but as these models do not have smooth tissue boundaries nor include tissue anisotropy, detail is sacrificed for the sake of time. The goal of this study was to provide for one model the most accurate predictions possible. The detailed description of the model creation process presented in this paper, a scheme that consists almost completely out of freely available software, can guide other investigators in creating similar models and extend the current knowledge base.

Although the model presented here contains much detail, shortcomings do surely exist. To prevent gray matter and skull surfaces intersecting, the brain of our model had to be slightly scaled down, leading to a slightly enlarged CSF volume. Also, our model does not include air compartments. The rather large pockets of nonconducting air formed by the frontal sinuses could alter the results for configurations with an electrode over the supraorbital area. Because the sinuses were modeled as highly resistive compacta, and current flows out of an electrode mostly through the corners closest to the other electrode, mainly flowing over the sinuses for the configurations studied here, we do not expect this to strongly affect the results.

Simplifications were made in areas that were not expected to affect the results. The mouth and jaws were modeled as skin and thus in a real head these areas have a lower conductivity. As both electrodes are far away from this area for all configurations aimed at cerebral targets, this should not significantly alter the current flow in areas of interest. We tested this assumption by making the mouth area of the model non-conductive and repeating the simulations. For M1 stimulation, this resulted in a 1% increase in field strength both in the target area and in the complete brain. Even for cerebellar stimulation, where one electrode is located near the mouth, the differences were small: 1% in the target area and 2% in the cerebellum overall. These results show that a lack of detail in the mouth area does not significantly affect simulations.

Other models exist that explicitly model small structures like eye sclera and blood vessels [11], [12]. As it is nearly impossible to create closed surface meshes of such small structures, using a tetrahedral model almost automatically excludes them. This immediately leads to the question if such small structures could actually significantly affect simulations. We tested this by using a change in the conductivity of the smallest structure in our model as a representation of adding an even smaller structure with a different conductivity. Changing the conductivity of the eyes from 0.4 S/m [57], [37] to 1.5 S/m [50] for M1 stimulation leads to a change in the electric field strength of 0.6% in the target volume and 0.6% in the brain overall. This shows that the influence of small structures is only marginal and negligible compared to other unavoidable small modeling errors.

The neck muscles are mostly not included in tDCS volume conduction models. Because cerebellar stimulation might be affected by the neck muscles, they were included in the model presented here. Unfortunately, there is a large spread in the muscle conductivity values reported in literature, especially when the anisotropic nature of muscle tissue is taken into account [58], [59], [51]. We compared the results of the cerebellar configuration model using muscle conductivities at the edges of this range. Using a muscle conductivity of 0.16 S/m leads to an increase of 11% in the mean field strength in the target volume and 10% in the cerebellum overall, as compared to using 0.4 S/m. This shows that simulations of cerebellar tDCS could be improved by acquiring more knowledge on the conductivity of muscle tissue.

F. Optimizing electrode placement

Several computational studies have put forward novel methods to optimize electric field distributions resulting from tDCS. These studies use multiple small circular electrodes [60], [61], [62] and/or multi-channel stimulation patterns [61], [12], [62]. An improved configuration of two large electrodes, the most widely available setup of tDCS in practice, has only been provided for one cortical target [12].

Based on the combined findings of all targets in this study, we established the hypothesis that an electrode pair should be centered around the targeted area for optimal field strength. We developed and simulated new configurations based on this notion and found several that perform better than the standard configurations do. A configuration with the anode 5 cm posterior and the cathode 5 cm anterior to the motor cortex target site, resulted in a mean electric field strength in the M1 target volume of 2.6 mV/cm, which is 88% higher than was achieved with the standard configuration. The resulting field strength on the GM surface is displayed in Figure 7A, showing clearly that the electric field strength maximum lies around the targeted area. Figure 7 shows a similar improvement for the occipital cortex: the field strength in the target volume is 1.7 mV/cm, 94% higher than the result of the standard configuration. From our preliminary results it seems that in

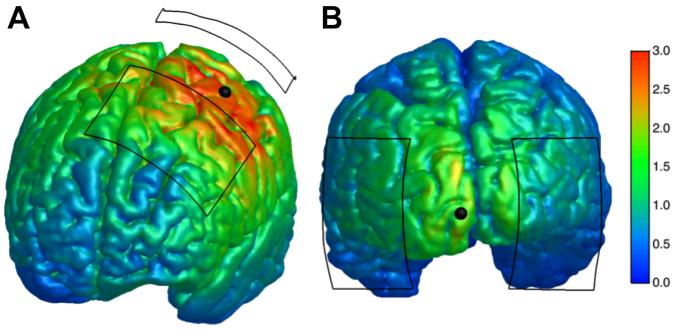

Fig. 7. Electric field strength $|\vec{E}|$ (mV/cm) on the surface of the GM for new configurations targeting the A) motor and B) occipital cortex. Scales are adjusted to allow comparison to the standard configurations in Figure 5. The black dot indicates the target of stimulation and the electrode-skin interface is outlined in black.

general (i.e. for any target), configurations with the electrodes on opposite sides of the target site lead to high field strengths in the target area. We were able to increase the field strength in the target volume with at least 70% for all five targets investigated here. Note that this includes the cerebellar target, which already seemed near-optimal.

Our next efforts are towards more precise substantiation of this hypothesis through optimization. Besides field strength, we will also optimize field strength perpendicular to the GM surface using the methods introduced here. In this study we introduced the concept of a meshed target volume to provide quantitative measures for the effectivity of stimulation and found that these analyses were successful in expressing a configurations ability to stimulate the target. Because these analyses allow for objective evaluation without the need for visual inspection, these methods are especially valuable for comparing large numbers of configurations for optimization purposes.

The effectiveness of the here-proposed configurations can be tested by comparing them with their respective standard configurations in an area-specific task. For the motor cortex, measurements of cortical excitability with TMS and EMG (size of motor-evoked potentials) could also be used. If such a new configuration were to lead to larger or more prolonged effects, this would not only provide evidence for an improved configuration, but also show that the field strength is the more important factor. On the other hand, if the new configurations were to perform worse, this would be evidence towards the theory that the direction of the field is the most important.

V. Conclusions

From the results of our study we conclude that 1) based on field strength, all five cerebral stimulation configurations studied here are not suited for their targets, 2) the commonly used configuration for cerebellum stimulation performs relatively well, 3) cerebellum stimulation needs higher input currents than does cerebral stimulation and 4) the direction of the field should be considered in all future studies. These results suggest space for improvement in the application and outcomes of tDCS and an important role for modeling in achieving these goals.

References

[1] M. Nitsche and W. Paulus, "Excitability changes induced in the human motor cortex by weak transcranial direct current stimulation," *J Physiol*, vol. 527, no. 3, pp. 633–9, 2000.

[2] M. Nitsche, M. Nitsche, C. Klein, F. Tergau, J. Rothwell, and W. Paulus, "Level of action of cathodal DC polarisation induced inhibition of the human motor cortex," *Clin Neurophysiol*, vol. 114, no. 4, pp. 600–4, 2003.

[3] M. Nitsche and W. Paulus, "Sustained excitability elevations induced by transcranial DC motor cortex stimulation in humans," *Neurology*, vol. 57, no. 10, pp. 1899–901, 2001.

[4] F. Hummel, P. Celnik, P. Giraux, A. Floel, W. Wu, C. Gerloff, and L. Cohen, "Effects of non-invasive cortical stimulation on skilled motor function in chronic stroke," *Brain*, vol. 128, no. 3, pp. 490–9, 2005.

[5] F. Fregni, P. Boggio, M. Santos, M. Lima, A. Vieira, S. Rigonatti, M. Silva, E. Barbosa, M. Nitsche, and A. Pascual-Leone, "Noninvasive cortical stimulation with transcranial direct current stimulation in Parkinsons disease," *Mov Disord*, vol. 21, no. 10, pp. 1693–702, 2006.

[6] A. Brunoni, R. Ferrucci, M. Bortolomasi, M. Vergari, L. Tadini, P. Boggio, M. Giacopuzzi, S. Barbieri, and A. Priori, "Transcranial direct current stimulation (tDCS) in unipolar vs. bipolar depressive disorder," *Prog Neuropsychopharmacol Biol Psychiatry*, vol. 35, no. 1, pp. 96–101, 2011.

[7] A. Javadi and P. Cheng, "Transcranial direct current stimulation (tDCS) enhances reconsolidation of long-term memory," *Brain Stimul*, vol. 6, no. 4, pp. 668–74, 2012.

[8] N. Metuki, T. Sela, and M. Lavidor, "Enhancing cognitive control components of insight problems solving by anodal tDCS of the left dorsolateral prefrontal cortex," *Brain Stimul*, vol. 5, no. 2, pp. 110–5, 2012.

[9] S. Rampersad, D. Stegeman, and T. Oostendorp, "Single-layer skull approximations perform well in transcranial direct current stimulation modeling," *IEEE Trans Neural Syst Rehabil Eng*, vol. AOP, 2012.

[10] H. Suh, W. Lee, and T. Kim, "Influence of anisotropic conductivity in the skull and white matter on transcranial direct current stimulation via an anatomically realistic finite element head model," *Phys Med Biol*, vol. 57, no. 21, pp. 6961–80, 2012.

[11] M. Parazzini, S. Fiocchi, and P. Ravazzani, "Electric field and current density distribution in an anatomical head model during transcranial direct current stimulation for tinnitus treatment," *Bioelectromagnetics*, vol. 33, no. 6, pp. 476–87, 2012.

[12] R. Sadleir, T. Vannorsdall, D. Schretlen, and B. Gordon, "Target optimization in transcranial direct current stimulation," *Front Psychiatry*, vol. 3, no. 90, 2012.

[13] A. Datta, V. Bansal, J. Diaz, J. Patel, D. Reato, and M. Bikson, "Gyri-precise head model of transcranial direct current stimulation: Improved spatial focality using a ring electrode versus conventional rectangular pad," *Brain Stimul*, vol. 2, no. 4, pp. 201–7, 2009.

[14] M. Windhoff, A. Opitz, and A. Thielscher, "Electric field calculations in brain stimulation based on finite elements: An optimized processing pipeline for the generation and usage of accurate individual head models," *Hum Brain Mapp*, vol. 34, no. 4, pp. 923–35, 2013.

[15] S. Shahid, P. Wen, and T. Ahfock, "Numerical investigation of white matter anisotropic conductivity in defining current distribution under tdcs," *Comput Methods Programs Biomed*, vol. 109, no. 1, pp. 48–64, 2013.

[16] L. Bradnam, C. Stinear, P. Barber, and W. Byblow, "Contralesional hemisphere control of the proximal paretic upper limb following stroke," *Cereb Cortex*, vol. 22, no. 11, pp. 2662–71, 2012.

[17] A. Zandieh, S. Parhizgar, M. Fakhri, M. Taghvaei, S. Miri, A. Shahbabaie, S. Esteghamati, and H. Ekhtiari, "Modulation of cold pain perception by transcranial direct current stimulation in healthy individuals," *Neuromodulation*, vol. 16, no. 4, pp. 345–8, 2012.

[18] J. Grundey, N. Thirugnanasambandam, K. Kaminsky, A. Drees, A. Skwirba, N. Lang, W. Paulus, and M. Nitsche, "Neuroplasticity in cigarette smokers is altered under withdrawal and partially restituted by nicotine exposition," *J Neurosci*, vol. 32, no. 12, pp. 4156–62, 2012.

[19] R. Montenegro, A. Okano, F. Cunha, J. Gurgel, E. Fontes, and P. Farinatti, "Prefrontal cortex transcranial direct current stimulation associated with aerobic exercise change aspects of appetite sensation in overweight adults," *Appetite*, vol. 58, no. 1, pp. 333–8, 2012.

[20] C. Loo, A. Alonzo, D. Martin, P. Mitchell, V. Galvez, and P. Sachdev, "Transcranial direct current stimulation for depression: 3-week, randomised, sham-controlled trial," *Br J Psychiatry*, vol. 200, no. 1, pp. 52–9, 2012.

[21] M. Nitsche, J. Koschack, H. Pohlers, S. Hullemann, W. Paulus, and S. Happe, "Effects of frontal transcranial direct current stimulation on emotional state and processing in healthy humans," *Front Psychiatry*, vol. 3, no. 58, 2012.

[22] H. Maeoka, A. Matsuo, M. Hiyamizu, S. Morioka, and H. Ando, "Influence of transcranial direct current stimulation of the dorsolateral prefrontal cortex on pain related emotions: A study using electroencephalographic power spectrum analysis," *Neurosci Lett*, vol. 512, no. 1, pp. 12–6, 2012.

[23] P. Boggio, S. Zaghi, A. Villani, S. Fecteau, A. Pascual-Leone, and F. Fregni, "Modulation of risk-taking in marijuana users by transcranial direct current stimulation (tDCS) of the dorsolateral prefrontal cortex (DLPFC)," *Drug Alcohol Depend*, vol. 112, no. 3, pp. 220–5, 2010.

[24] A. Brunoni, M. Vanderhasselt, P. Boggio, F. Fregni, E. Dantas, J. Mill, P. Lotufo, and I. Benseor, "Polarity- and valence-dependent effects of prefrontal transcranial direct current stimulation on heart rate variability and salivary cortisol," *Psychoneuroendocrinology*, vol. 38, no. 1, pp. 58–66, 2013.

[25] E. Frank, M. Schecklmann, M. Landgrebe, J. Burger, P. Kreuzer, T. Poeppl, T. Kleinjung, G. Hajak, and B. Langguth, "Treatment of chronic tinnitus with repeated sessions of prefrontal transcranial direct current stimulation: Outcomes from an open-label pilot study," *J Neurol*, vol. 259, no. 2, pp. 327–33, 2012.

[26] P. Marangolo, C. Marinelli, S. Bonifazi, V. Fiori, M. Ceravolo, L. Provinciali, and F. Tomaiuolo, "Electrical stimulation over the left inferior frontal gyrus (IFG) determines long-term effects in the recovery of speech apraxia in three chronic aphasics," *Behav Brain Res*, vol. 225, no. 2, pp. 498–504, 2011.

[27] T. Ditye, L. Jacobson, V. Walsh, and M. Lavidor, "Modulating behavioral inhibition by tDCS combined with cognitive training," *Exp Brain Res*, vol. 219, no. 3, pp. 363–8, 2012.

[28] A. Pisoni, C. Papagno, and Z. Cattaneo, "Neural correlates of the semantic interference effect: New evidence from transcranial direct current stimulation," *Neuroscience*, vol. 223, pp. 56–67, 2012.

[29] P. Enticott, S. Arnold, B. Fitzgibbon, K. Hoy, D. Susilo, and P. Fitzgerald, "Transcranial direct current stimulation (tDCS) of the inferior frontal gyrus disrupts interpersonal motor resonance," *Neuropsychologia*, vol. 50, no. 7, pp. 1628–31, 2012.

[30] M. Siniatchkin, M. Sendacki, F. Moeller, S. Wolff, O. Jansen, H. Siebner, and U. Stephani, "Abnormal changes of synaptic excitability in migraine with aura," *Cereb Cortex*, vol. 22, no. 10, pp. 2207–16, 2012.

[31] E. Plow, S. Obretenova, M. Jackson, and L. Merabet, "Temporal profile of functional visual rehabilitative outcomes modulated by transcranial direct current stimulation," *Neuromodulation*, vol. 15, no. 4, pp. 367–73, 2012.

[32] J. Galea, G. Jayaram, L. Ajagbe, and P. Celnik, "Modulation of cerebellar excitability by polarity-specific noninvasive direct current stimulation," *J Neurosci*, vol. 29, no. 28, pp. 9115–22, 2009.

[33] G. Jayaram, B. Tang, R. Pallegadda, E. Vasudevan, P. Celnik, and A. Bastian, "Modulating locomotor adaptation with cerebellar stimulation," *J Neurophysiol*, vol. 107, no. 11, pp. 2950–7, 2012.

[34] C. Im, J. Park, M. Shim, W. Chang, and Y. Kim, "Evaluation of local electric fields generated by transcranial direct current stimulation with an extracephalic reference electrode based on realistic 3D body modeling," *Phys Med Biol*, vol. 57, no. 8, pp. 2137–50, 2012.

[35] R. Salvador, A. Mekonnen, G. Ruffini, and P. Miranda, "Modeling the electric field induced in a high resolution realistic head model during transcranial current stimulation," in *Conf Proc IEEE Eng Med Biol Soc*, 2010, pp. 2073–6.

[36] T. Wagner, F. Fregni, S. Fecteau, A. Grodzinsky, M. Zahn, and A. Pascual-Leone, "Transcranial direct current stimulation: A computer-based human model study," *Neuroimage*, vol. 35, no. 3, pp. 1113–24, 2007.

[37] M. Halko, A. Datta, E. Plow, J. Scaturro, M. Bikson, and L. Merabet, "Neuroplastic changes following rehabilitative training correlate with regional electrical field induced with tDCS," *Neuroimage*, vol. 57, no. 3, pp. 885–91, 2011.

[38] S. Wagner, S. Rampersad, U. Aydin, J. Vorwerk, T. Oostendorp, T. Neuling, C. Hermann, D. Stegeman, and C. Wolters, "Investigation of tDCS volume conduction effects in a highly realistic head model," *J Neural Eng*, vol. 11, p. 016002, 2013.

[39] P. Basser, J. Mattiello, and D. LeBihan, "MR diffusion tensor spectroscopy and imaging," *Biophys J*, vol. 66, no. 1, pp. 259–67, 1994.

[40] D. Tuch, V. Wedeen, A. Dale, J. George, and J. Belliveau, "Conductivity tensor mapping of the human brain using diffusion tensor MRI," *Proc Natl Acad Sci U S A*, vol. 98, no. 20, pp. 11 697–701, 2001.

[41] A. Chaturvedi, C. Butson, S. Lempka, S. Cooper, and C. McIntyre, "Patient-specific models of deep brain stimulation: influence of field model complexity on neural activation predictions," *Brain Stimul*, vol. 15, no. 1, pp. 159–66, 2010.

[42] L. Vese and T. Chan, "A multiphase level set framework for image segmentation using the Mumford and Shah model," *Int J Comput Vis*, vol. 50, no. 3, p. 27193, 2002.

[43] G. Taubin, "A signal processing approach to fair surface design," in *Proc Conf Comput Graph Inter Techn*, 1995, pp. 351–8.

[44] Q. Fang and D. Boas, "Tetrahedral mesh generation from volumetric binary and gray-scale images," in *Proc IEEE Int Symp Biomed Imaging*, 2009, pp. 1142–1145.

[45] A. Leemans and J. DK, "The B-matrix must be rotated when correcting for subject motion in DTI data," *Magn Reson Med*, vol. 61, no. 6, pp. 1336–49, 2009.

[46] L. Ruthotto, H. Kugel, J. Olesch, B. Fischer, J. Modersitzki, M. Burger, and C. Wolters, "Diffeomorphic susceptibility artifact correction of diffusion-weighted magnetic resonance images," *Phys Med Biol*, vol. 57, no. 18, pp. 5715–31, 2012.

[47] T. Behrens, M. Woolrich, M. Jenkinson, H. Johansen-Berg, R. Nunes, S. Clare, P. Matthews, J. Brady, and S. Smith, "Characterization and propagation of uncertainty in diffusion-weighted MR imaging," *Magn Reson Med*, vol. 50, no. 5, pp. 1077–88, 2003.

[48] A. Opitz, M. Windhoff, R. Heidemann, R. Turner, and A. Thielscher, "How the brain tissue shapes the electric field induced by transcranial 2 magnetic stimulation," *Neuroimage*, vol. 58, no. 3, pp. 849–59, 2011.

[49] M. Akhtari, H. Bryant, A. Mamelak, E. Flynn, L. Heller, J. Shih, M. Mandelkern, A. Matlachov, R. DM, E. Best, M. DiMauro, R. Lee, and W. Sutherling, "Conductivities of three-layer live human skull," *Brain Topogr*, vol. 14, no. 3, pp. 151–167, 2002.

[50] M. Nadeem, T. Thorlin, O. Gandhi, and M. Persson, "Computation of electric and magnetic stimulation in human head using the 3-D impedance method," *IEEE Trans Biomed Eng*, vol. 50, no. 7, pp. 900–7, 2003.

[51] T. Faes, H. van der Meij, J. de Munck, and R. Heethaar, "The electric resistivity of human tissues (100 Hz-10 MHz): a meta-analysis of review studies," *Physiol Meas*, vol. 20, no. 4, pp. R1–10, 1999.

[52] W. Rushton, "Effect upon the threshold for nervous excitation of the length of nerve exposed and the angle between current and nerve," *J Physiol*, vol. 63, no. 4, pp. 357–77, 1927.

[53] T. Radman, A. Datta, R. Ramos, J. Brumberg, and M. Bikson, "One-dimensional representation of a neuron in a uniform electric field," in *Conf Proc IEEE Eng Med Biol Soc*, 2009, pp. 6481–4.

[54] R. Heidemann, D. Porter, A. Anwander, T. Feiweier, K. Heberlein, T. Knsche, and R. Turner, "Diffusion imaging in humans at 7T using readout-segmented EPI and GRAPPA," *Magn Reson Med*, vol. 64, no. 1, pp. 9–14, 2010.

[55] P. Miranda, M. Lomarev, and M. Hallett, "Modeling the current distribution during transcranial direct current stimulation," *Clin Neurophysiol*, vol. 117, no. 7, pp. 1623–1629, 2006.

[56] M. Hamada, G. Strigaro, N. Murase, A. Sadnicka, J. Galea, M. Edwards, and J. Rothwell, "Cerebellar modulation of human associative plasticity," *J Physiol*, vol. 590, no. 10, pp. 2365–74, 2012.

[57] A. Datta, J. Baker, M. Bikson, and J. Fridriksson, "Individualized model predicts brain current flow during transcranial direct-current stimulation treatment in responsive stroke patient," *Brain Stimul*, vol. 4, no. 3, pp. 169–74, 2011.

[58] C. Gabriel, S. Gabriel, and E. Corthout, "The dielectric properties of biological tissues: I. Literature survey," *Phys Med Biol*, vol. 41, no. 11, pp. 2231–49, 1996.

[59] S. Gabriel, R. Lau, and C. Gabriel, "The dielectric properties of biological tissues: II. Measurements in the frequency range 10 Hz to 20 GHz," *Phys Med Biol*, vol. 41, no. 11, pp. 2251–69, 1996.

[60] J. Park, S. Hong, D. Kim, M. Suh, and C. Im, "A novel array-type transcranial direct current stimulation (tDCS) system for accurate focusing on targeted brain areas," *IEEE Trans Magn*, vol. 47, no. 5, pp. 882–5, 2011.

[61] J. Dmochowski, A. Datta, M. Bikson, Y. Su, and L. Parra, "Optimized multi-electrode stimulation increases focality and intensity at target," *J Neural Eng*, vol. 8, no. 4, p. 046011, 2011.

[62] H. Kuo, M. Bikson, A. Datta, P. Minhas, W. Paulus, M. Kuo, and M. Nitsche, "Comparing cortical plasticity induced by conventional and high-definition 4 x 1 ring tDCS: a neurophysiological study," *Brain Stimul*, vol. 6, no. 4, pp. 644–8, 2013.